NASA TECHNICAL NOTE

NASA TN D-6350

a. 1

NASA TN D-6350

TECH LIBRARY KAFB, NM
0132865

LOAN COPY: RETURN
AFWL (DOGL)
KIRTLAND AFB, N. M

CRITICAL SPEEDS OF A ROTOR IN RIGIDLY MOUNTED, EXTERNALLY PRESSURIZED, AIR-LUBRICATED BEARINGS

by Robert E. Cunningham and Edward J. Gunter, Jr.

Lewis Research Center
Cleveland, Ohio 44135

NATIONAL AERONAUTICS AND SPACE ADMINISTRATION • WASHINGTON, D. C. • MAY 1971

TECH LIBRARY KAFB, NM
0132865

1. Report No.	2. Government Accession No.	3. Recipient's Catalog No.
NASA TN D-6350		

4. Title and Subtitle
CRITICAL SPEEDS OF A ROTOR IN RIGIDLY MOUNTED, EXTERNALLY PRESSURIZED, AIR-LUBRICATED BEARINGS

5. Report Date
May 1971

6. Performing Organization Code

7. Author(s)
Robert E. Cunningham and Edward J. Gunter, Jr.

8. Performing Organization Report No.
E-6134

10. Work Unit No.
129-03

9. Performing Organization Name and Address
Lewis Research Center
National Aeronautics and Space Administration
Cleveland, Ohio 44135

11. Contract or Grant No.

13. Type of Report and Period Covered
Technical Note

12. Sponsoring Agency Name and Address
National Aeronautics and Space Administration
Washington, D. C. 20546

14. Sponsoring Agency Code

15. Supplementary Notes

16. Abstract
Results of experiments conducted with rotors at speeds to 28 000 rpm indicate that rotor critical speeds for a two-bearing rotor system can be calculated quite accurately from rigid-body theory using the film stiffness as determined from zero-speed, load-eccentricity data. Results of a flexible rotor analysis show that accurate critical-speed predictions are possible even for the conical mode, when the bearing forces are assumed to act in a single plane.

17. Key Words (Suggested by Author(s))
Bearings, Critical speeds, Rigid rotor, Externally pressurized, Air lubricated, Radial bearings, Rigid support, Gas film stiffness, Instability threshold, Fractional frequency whirl

18. Distribution Statement
Unclassified - unlimited

19. Security Classif. (of this report)	20. Security Classif. (of this page)	21. No. of Pages	22. Price*
Unclassified	Unclassified	27	$3.00

*For sale by the National Technical Information Service, Springfield, Virginia 22151

CRITICAL SPEEDS OF A ROTOR IN RIGIDLY MOUNTED, EXTERNALLY PRESSURIZED, AIR-LUBRICATED BEARINGS

by Robert E. Cunningham and Edward J. Gunter, Jr.*

Lewis Research Center

SUMMARY

Tests on a $2\frac{1}{2}$-inch (6.3-cm) diameter, 18-inch (46-cm) long rotor operating in two externally pressurized gas bearings show that critical speeds can be calculated quite accurately from rigid-body theory using the film stiffness as determined from load-against-eccentricity data at zero speed. Static film stiffnesses were found to have a maximum value at zero eccentricity ratio and then to decrease nonlinearly with increasing eccentricity ratio.

Results of a flexible rotor analysis show that the accuracy of critical-speed predictions is not compromised when the bearing forces are assumed to act in one plane (lumped bearing model) rather than as distributed forces over the entire bearing length.

Critical-speed peak amplitudes were observed to decrease generally for decreasing supply pressure ratios, suggesting that greater damping exists in the gas film at lower film pressures. The instability threshold speeds always occurred above the system critical speeds over the range of supply pressure ratios from 1.7 to 7.4. The frequency of rotor motion at a supply pressure ratio of 4.5 was found to be 0.747 that of the rotor angular speed.

INTRODUCTION

Rotating machinery of all types produce vibrations, motions which impair performance and result in a reduction in the useful life. The most common vibration encountered is the whirling motion of a shaft about its longitudinal axis due to unbalance. This is known as synchronous whirl because the frequency coincides with the shaft angular speed. Large amplitudes of motion may occur when the rotor angular speed coincides with that

*Professor of Mechanical Engineering, University of Virginia, Charlottesville, Va.

of the lateral natural frequency of the shaft in its bearings, commonly referred to as the system "critical speed(s)." The relatively large amplitudes of motion generated at a critical speed result in large forces transmitted to the bearings (ref. 1). The rotor amplitudes of motion encountered at the critical speeds are a function of the rotor unbalance and the bearing damping in the system (refs. 1 and 2). By careful balancing, the unbalance response at the critical speeds may be reduced or eliminated.

When the rotor is operated substantially above the first system critical speed, a self-excited nonsynchronous precession (fractional frequency whirl) may occur (ref. 3). This effect in the hybrid bearing is caused by the hydrodynamic action of the bearings (ref. 4) and is not a function of unbalance. Various theoretical investigations on stability have shown that the rotor precession rate and the stability threshold are closely related to the first critical speed (refs. 4 and 5). For example, if the bearing supply pressure is decreased, the effective stiffness of the bearings decreases. This causes a reduction in the rotor critical speeds and a corresponding reduction in the threshold speed. If the bearing supply pressure is completely shut off, the effective radial bearing stiffness due to external pressurization is zero, and the vertical rotor will be unstable at all speeds and will whirl at a frequency equal to one-half rotor speed (ref. 6).

In order to produce a smooth-running machine with minimum vibration amplitudes, operation at or near system critical speeds must be avoided and operation must be limited to speeds below the threshold of instability. For example, in the design of small, high-speed turbomachinery such as the Brayton gas cycle system, precision balancing is essential to permit operation above the system's critical speeds without damaging the gas-lubricated journal bearings, whose clearances are very small.

The objectives of this investigation are as follows: (1) to operate a vertical rotor in externally pressurized air bearings through the critical speeds and up to the instability threshold; (2) to investigate the influence of the bearing supply pressure, clearance, and eccentricity ratio on bearing film stiffness; and (3) to compare the observed critical speeds with the calculated values based on the zero-speed stiffness data.

The experimental results reported in this investigation were obtained over a speed range from zero to 28 000 rpm. Supply pressure ratios P_o/P_a to the bearings varied from 1.7 to 7.4, corresponding to pressures P_o of 24.6 and 107 psia (170 and 738 kN/m^2), respectively. The air-lubricated journal bearings were 2.5 inches (6.3 cm) in diameter by 3.75 inches (9.5 cm) long and had two planes of six equally spaced orifices. Two sets of bearings were used, set A having average assembled radial clearances c of 0.0014 inch (0.036 mm) in the upper and lower bearings. Set B had average assembled radial clearances of 0.0008 inch (0.020 mm) in the upper bearing and 0.0009 inch (0.023 mm) in the lower bearing. The average orifice diameter d_o for large-clearance bearings (set A) was 0.022 inch (0.56 mm), and 0.013-inch (0.33-mm) diameter orifices were used in bearing set B.

The tests were performed in atmospheric-pressure air at ambient temperatures from 68° to 72° F (293 to 296 K).

APPARATUS

Test Rig

The test rig used in this investigation is shown in figure 1. There were two externally pressurized air bearings, whose centerline distance (span) was 8 inches (20.3 cm). These bearings located a constant-diameter rotor in a vertical position. The upper bearing could be adjusted both laterally and angularly to permit alinement with the lower bearing in its housing. An externally pressurized, recess-pocket, thrust bearing supported the weight of the steel test rotors.

Unidirectional radial loads up to 300 pounds (1340 N) were applied to the rotor by an externally pressurized load shoe attached to a pneumatic load cylinder through a pivot assembly, see schematic in figure 1. The load was applied equidistant between the two bearings so that each received the same amount of radial load.

Pressurized air from two nozzles impinging on a set of slots milled into the rotor surface at the upper end drove the rotor up to speed. A like set of slots at the lower end, but machined in the opposite direction, served as a brake to reduce rotor speed rapidly.

Test Bearings and Rotors

One of the bearings used in the investigation is shown alongside a steel test rotor in figure 2. The bearings have nominal diameters of $2\frac{1}{2}$ inches (6.3 cm) and are $3\frac{3}{4}$ inches (9.5 cm) long. They are made of SAE-68 B, cast aluminum bronze, and were finish-machined round and concentric to 40 microinches (1 μm) before installation in the test apparatus.

Two sets of bearings were tested: set A which had a nominal diametral clearance c_d of 0.003 inch (0.076 mm), and set B which had a nominal diametral clearance of 0.002 inch (0.051 mm). The average measured, preassembled, diametral clearances are listed in table I.

Each bearing has two rows of six equally spaced orifices for a total of 12 per bearing. The rows of orifices are located one-quarter of the way in from the bearing ends, as shown in figure 3. Orifice sizes used are listed in table I.

Two uniform, $2\frac{1}{2}$-inch (6.3-cm) diameter, solid steel rotors were used to obtain the tabulated results of this investigation. Several preliminary trial runs were also made with a hollow steel rotor having the same overall dimensions. These 18-inch (46-cm) long rotors were machined round within 20 microinches (0.5 μm) and concentric within 50 microinches (1.3 μm). The rotors were made from consumable-electrode-vacuum-melt SAE-52100 steel. After heat treatment, the surfaces were chrome plated. Table II lists the pertinent physical constants for three rotors used in this investigation.

Instrumentation

Radial rotor displacement was detected by two noncontacting capacitance probes mounted at right angles to each other and located outboard of each bearing, as shown in the schematic of figure 1. Voltage output from the probes which is proportional to displacement could be fed to either a frequency-modulated (FM) tape recorder, X-Y curve tracing oscilloscopes, or an X-Y plotter. All three data-reading schemes were used in determining critical speeds. Probe voltage output was measured with a digital voltmeter capable of 1-millivolt discrimination, which corresponds to a distance of 5 microinches (0.13 μm). This instrument was used in determining rotor eccentricity in the load-eccentricity tests.

Pressures to the load cylinder were read on a Bourdon tube gage (0.5 percent accuracy) and then converted to pounds of force from calibration curves. Supply pressures to the bearings were measured by strain gage transducers (accurate to 0.1 percent) and their output read on a digital voltmeter.

A solid-state electronic controller was used to regulate turbine air supply and to maintain a preset rotor speed to within 0.5 percent. Both inductive and photoelectric sensors, in conjunction with digital counters, were used to monitor speed.

PROCEDURE

Assembled diametral bearing clearances c_d were measured before each test. This was accomplished by first turning off the air supply to both test bearings, permitting an unrestricted movement of the rotor within the clearance circle of each bearing. The rotor was displaced along two perpendicular axes, one of which (Y axis) was coincident with the applied load axis. Total X and Y displacements (diametral clearances) were measured by noncontacting capacitance probes as described in the section APPARATUS under Instrumentation. These average assembled diametral clearances are listed in table I. The difference between the preassembled and assembled diametral clearances

shown in table I is due to misalinement between the two bearings. The greater misalinement occurred with bearing set B, and figure 4 illustrates schematically why the assembled clearances are somewhat less than the preassembled clearances. When the rotor was displaced along the X and Y axes, the resulting measurements differed appreciably, as shown in figure 4. Instead of the rotor center describing a circular path when moved by hand, it actually followed an elliptical one. Each of the assembled clearances listed in table I is the average of the X- and Y-axes clearances illustrated in figure 4.

Since it was known that the bearings were machined round to begin with, one possible explanation is an angular misalinement of top and bottom bearings. This is again illustrated schematically in the section views of bearings and rotor in figure 4. The X-Y curve tracing oscilloscopes connected to the orthogonally mounted probes at each bearing also displayed a similar elliptical path.

The orthogonal displacement readings obtained by the method described were used in conjunction with the oscilloscope displays to locate the concentric rotor or the zero eccentricity position. These readings were then compared with the zero load position of the rotor in each of its journal bearings when the air was turned back on. Establishing this initial rotor position within the bearing clearance was most important for the load-eccentricity tests. These tests consisted of applying a known load to the rotor by means of the pneumatic cylinder and pressurized load shoe and observing the resulting displacements.

For the critical-speed tests a particular supply pressure was set and the rotor angular speed was gradually increased. The amplitude and speed were automatically recorded on a calibrated X-Y plotter. Tests were terminated when the nonsynchronous (fractional frequency) whirl threshold was observed. Phase shifts associated with the critical speeds were also monitored by noting the relative position of a blip on the oscilloscope trace produced by a marker on the rotor surface passing underneath the capacitance probes. A Polaroid camera attached to the scope face was used to photograph rotor motions.

RESULTS AND DISCUSSION

The experimental results of this investigation were obtained with a $2\frac{1}{2}$-inch (6.3-cm) diameter, 18-inch (46-cm) long, 24.6-pound (11.1-kg) steel rotor operated vertically in two $3\frac{3}{4}$-inch (9.5-cm) long, externally pressurized, air-lubricated bearings to a speed of 28 000 rpm. Observed critical speeds plus static load-eccentricity and stiffness data are given in table III and in figures 5 to 14. Bearing supply pressure ratios P_o/P_a were varied from 1.7 to 7.4 and assembled radial clearances of 0.0014, 0.0009, and 0.0008 inch (0.036, 0.023, and 0.020 mm) were investigated.

Observed Critical Speeds

The observed critical speeds at different bearing supply pressure ratios are plotted in figures 5(a) and (b). The largest radial clearance investigated was 0.0014 inch (0.036 mm). This value is an average of the measured clearances for the upper and lower bearings of set A. The results are plotted in figure 5(a). At the first critical speed the motion of the rotor can be described as conical, while at the second critical speed it is cylindrical. These rigid-body mode shapes are pictured schematically alongside each curve. Which critical speed occurs first is a function of rotor geometry and the bearing span S. The critical speeds are seen to increase with increasing supply pressure ratios. Since critical speed is a function of film stiffness and stiffness for this type of a bearing increases with supply pressure (refs. 7 and 8), this sort of trend would be anticipated.

When smaller clearances were tested, namely 0.009 and 0.008 inch (0.023 and 0.020 mm), bearing set B, only the first (or conical) mode was observed. This peculiarity may be due to some slight amount of misalinement between the two bearings, as described in the section PROCEDURE and shown schematically in figure 4. Figure 5(b) also shows that the conical (or first critical) speed is increasing with increasing supply pressure ratio.

Observed Instability Threshold Speeds

The uppermost curves in figures 5(a) and (b) are the threshold speeds for nonsynchronous rotor motion. This is a self-excited orbital motion which occurs in plain cylindrical, self-acting bearings with a frequency equal to 0.5 that of the rotor angular speed (ref. 6). The frequency of precession measured was 0.747 that of the rotor angular speed at a supply pressure ratio of 4.5. This value would probably approach 0.5 as the supply pressure ratio approached 1. Reference 3 shows that higher values occur in externally pressurized bearings than in plain cylindrical self-acting bearings. In all tests conducted this nonsynchronous threshold speed, which always occurred above the system critical speeds, became the limiting operating speed because of the rapid increase in orbital amplitude. This increase was greatest at the lowest supply pressure, where a correspondingly weaker film stiffness exists. The lower film stiffness produces a smaller restoring force opposing the centrifugal force of the whirling rotor.

Peak-To-Peak Rotor Amplitudes

The peak-to-peak amplitudes as a function of rotor speed are shown in figures 6 and 7. These are traces produced on an X-Y plotter. The ordinate axis is the rotor amplitude as measured by a capacitance distance probe located approximately 3/8 inch (9.5 mm) outboard of each bearing. As shown in figure 6 two critical speeds are easily distinguishable for the four different supply pressures. A greater amplitude is seen for the upper bearing in each case, and this is probably due to a greater amount of unbalance at the upper end of the rotor than at the lower end. In figure 7 there is only one distinct buildup in amplitude. The two rigid-body modes evidently occur so close together the second (or cylindrical) mode is masked by the first (or conical) mode. A greater degree of misalinement was present in the smaller-clearance bearings (set B) than was present in set A at assembly.

There is a general increase in the critical-speed amplitudes with increasing supply pressure ratio at both upper and lower bearings. The rate of increase and decrease is also much greater at the higher supply pressure ratios. This suggests that somewhat more damping is present in the film at the lower supply pressure ratios. The gradually rounded protuberances in figures 7(a) and (b) resemble the classic amplitude-frequency curves for a highly damped spring mass system (ref. 9).

The insets of figure 6(d) show rotor motion as it appears for different speeds, up to and including the instability threshold. The two orthogonally positioned "blips" seen in the insets were produced by a single reference mark machined into the surface of the rotor. The mark is positioned so that it passes directly beneath the two capacitance probes which are located just outboard of a bearing. It is interesting to note the change in appearance of the reference marks from inset 3 to inset 4. In addition to a smaller orbit size at position 4, there has been a 180° phase shift, as occurs when the first critical speed has been passed. The smaller orbit is due to the rotor spinning about its mass center rather than its geometric center.

Inset 5 illustrates nonsynchronous orbital precession. It is generally distinguished from the synchronous motion by a characteristic inward-facing cusp (ref. 5).

Bearing Film Stiffness

In order to calculate rotor critical speeds, bearing stiffnesses must be known. These stiffnesses were determined from load-against-eccentricity tests at different supply pressure ratios. The results of such tests, at zero rotor angular speed, are plotted in figures 8 and 9. Supply pressure ratios P_o/P_a investigated were 1.76 to 7.4, and

radial clearances were 0.0008, 0.0009, and 0.0014 inch (0.020, 0.023, and 0.036 mm), respectively. From these data and a least-squares error curve fit, computer program values of stiffness at eccentricity ratios were obtained and are plotted in figures 10 and 11. Two curves at each supply pressure have been plotted. The solid line is stiffness obtained by differentiating the polynomial fitted to the load-displacement data by the curve-fit program. The dashed lines represent the stiffness obtained by dividing the load at a given eccentricity by that value of the eccentricity. This method yields a larger value of stiffness (except at zero eccentricity ratio) than that obtained by differentiation, particularly at the higher eccentricity ratios. However, values of the stiffness obtained by dividing the load by the eccentricity approach more closely the actual conditions that exist when a rotor precesses in a finite orbit at synchronous speed about the bearing center. It is also to be expected that a greater stiffness occurs at this condition because of squeeze film effects (ref. 10). Film stiffnesses for a rotating shaft will also be somewhat greater due to an overall increase in the film pressure from self-acting effects (ref. 7). These plots show that maximum stiffness occurs at zero eccentricity ratios and that the stiffness decreases nonlinearly with increasing eccentricity ratio. This is characteristic of the nonrecessed, stationary, externally pressurized air bearing (ref. 8). The plots of figures 10 and 11 show that stiffness increases with increasing bearing supply pressure and decreasing clearance. The rate of increase becomes clearer when, at a given eccentricity, the stiffness is plotted as a function of supply pressure (figs. 12(a) and (b)). At eccentricity ratios $\epsilon = 0$ and $\epsilon = 0.3$ the stiffness increases quite rapidly to a pressure ratio of about 4. Above this value the stiffness is still increasing but at a slower rate. These plots also show the higher stiffness that can be obtained by reducing the bearing radial clearance.

Critical-Speed Analysis

In order to examine the influence of rotor flexibility on the critical speeds, the rotor critical speeds were calculated by a matrix transfer method. The rotor was divided into seven mass stations, as shown in figure 13(a), in which the bearing stiffness characteristics were lumped into a single plane acting at the centerplanes of the top and bottom bearings. The critical speeds were calculated for a stiffness range of 50 000 to 500 000 pounds per inch (87.5 to 875 kN/cm). The values of the critical speeds are shown plotted against bearing stiffness as the solid lines in figure 14. From the observation of the mode shapes corresponding to the critical speeds, it was concluded that the first mode is a rigid-body conical mode in which the rotor motions at the bearings are out of phase. The second mode corresponded to a rigid-body cylindrical mode in which these motions are in phase. The third critical speed, which is not shown in figure 14, corresponds to

the free bending mode and has a value of 82 000 rpm. At this speed the mode shape is largely unaffected by the bearing characteristics and hence the third critical speed is approximately constant for the stiffness range of 50 000 to 500 000 pounds per inch (87.5 to 875 kN/cm). Thus, from the analysis of the rotor mode shapes it was concluded that, for the range of bearing stiffnesses considered and for the operating speed range, rotor flexibility has a negligible effect on the first two critical speeds.

The externally pressurized bearings are a total of 7.50 inches (19 cm) long, which for the 18-inch (46-cm) rotor represents 42 percent of its length. Therefore, it is of considerable importance to determine whether the bearing characteristics can be assumed to be acting at a single plane at the bearing centerplane, or whether the bearing must be treated as a distributed system acting over the entire bearing length. The rotor critical speeds were recalculated using a nine-mass-station model, as shown in figure 13(b), in which the bearing characteristics were distributed into two planes. The resulting critical speeds from this system are shown as dashed lines in figure 14.

Values of the second (or cylindrical) critical speed calculated with the distributed-bearing assumption are identical to those calculated for the lumped-bearing assumption. This is to be expected since the rotor motions at the bearings are in phase, causing the same effective bearing reactions to occur in both cases.

The mode shape for the first critical speed is conical and thus the distributed-bearing assumptions will introduce an angular stiffness into the system. This will cause restoring moments to act on the shaft which are not present in the lumped-bearing calculations.

Therefore, as expected, the distributed-bearing assumption results in the calculation of a slightly higher first critical speed because of the angular stiffness effect introduced. From a practical standpoint, however, the angular stiffness effect or moments exerted by the bearings on the rotor are negligible, and the bearing forces may be treated as acting in planes normal to the rotor axis at the bearing centers. A calculation was also performed for a 13-mass-station rotor, in which the bearing characteristics were distributed in four planes for each bearing. There was no noticeable difference between the two-plane bearing assumption and the four-plane assumption.

Thus from the analysis of the flexible rotor critical speeds and mode shapes, it has been determined that the critical speeds of the solid rotor may be accurately predicted by rigid-body theory. However, for the case of a hollow rotor model, there was some bending in the first two modes due to rotor flexibility and the end mass distribution. When the hollow rotor performance was simulated by the synchronous unbalance response program, it was seen that rotor unbalance could cause considerable shaft deformation and that the unbalance response of the hollow rotor cannot be accurately predicted by rigid-body theory. Conversely, this implies that if the hollow rotor is balanced as a rigid body, deflections at speed may be experienced due to rotor flexibility. Preliminary tests

with a hollow rotor confirm these conclusions. A certain amount of bending must have taken place since rubbing at the thrust face was in evidence.

SUMMARY OF RESULTS

Experimental results were obtained for a 2.5-inch (6.3-cm) diameter by 18-inch (46-cm) long steel rotor operated vertically in two 3.75-inch (9.5-cm) long, externally pressurized air bearings. Critical speeds and instability threshold speed data were obtained for two sets of bearings. Bearing set A had an average radial clearance of 0.0014 inch (0.036 mm), and bearing set B radial clearances of 0.0008 and 0.0009 inch (0.020 and 0.023 mm) in the upper and lower bearings, respectively. Supply pressures to the bearings were varied from 24.6 psia (17 kN/m^2) to 107 psia (738 kN/m^2), corresponding to pressure ratios P_o/P_a from 1.7 to 7.4. Speeds ranged from 0 to 28 000 rpm. Conclusions based on the results of this investigation are as follows:

1. The critical speeds for the two principal modes can be calculated quite accurately from rigid-body theory using stiffness values obtained by load-eccentricity data at zero speed.

2. Results of a flexible rotor analysis show that accurate predictions of critical speeds, even for the conical mode, are possible when the bearing forces are assumed to act in a single plane (lumped-bearing model).

3. Maximum static film stiffness for these bearings occurs when the rotor is in a concentric position (zero eccentricity) and decreases nonlinearly with increasing eccentricity ratio.

4. The critical-speed peak amplitudes observed at the lower supply pressure ratios are less than those at higher pressure ratios, suggesting that a greater amount of film damping exists at the lower supply pressures.

5. Bearing static film stiffness increases nonlinearly with increasing supply pressure ratio and with decreasing clearance.

6. Instability threshold speeds always occur above system critical speeds. The frequency of this instability at a supply pressure ratio of 4.5 was found to be 0.747 that of the rotor angular speed.

Lewis Research Center,
National Aeronautics and Space Administration,
Cleveland, Ohio, February 17, 1971,
129-03.

APPENDIX - SYMBOLS

c	bearing radial clearance for concentric rotor position, $c = R_b - R_r$, mm; in.
c_d	bearing diametral clearance, $c_d = 2c$, mm; in.
D	diameter, cm; in.
d_c	orifice curtain diameter, mm; in.
d_o	orifice diameter, mm; in.
e	rotor eccentricity, mm; in.
g	acceleration due to gravity, cm/sec^2; $in./sec^2$
I	mass moment of inertia, $kg\text{-}m^2$; $lb\text{-}in.\text{-}sec^2$
K	bearing film stiffness, $\Delta W/\Delta e$, N/cm; lbf/in.
k	bearing film stiffness, W/e, N/cm; lbf/in.
L	length, cm; in.
ℓ	orifice length, cm; in.
m	mass, kg; $lb\text{-}sec^2/in.$
N	rotor angular speed, rpm
n	number of orifices
P	pressure, N/m^2; psi
R	radius, cm; in.
S	axial distance between bearing centerlines, cm; in.
W	applied radial load, N; lbf/ft^2
x,y,z	coordinate axes
ϵ	eccentricity ratio, e/c
μ	absolute viscosity, $N\text{-}sec/m^2$; $lbf\text{-}ft^2\text{-}sec/in.^2$
ω	angular velocity, rad/sec

Subscripts:

a	atmospheric
b	bearing

CR1,CR2	first and second critical speeds
l	lower bearing
o	supply
p	polar
r	rotor
t	transverse
u	upper bearing
w	fractional frequency whirl threshold
x,y,z	coordinate axes

REFERENCES

1. Gunter, Edgar J., Jr.; and DeChoudhury, P.: Rigid Rotor Dynamics. NASA CR-1391, 1969, pp. 54-55.

2. Ono, Kyosuke: On the Allowable Unbalance of a Rigid Rotor Supported in Externally Pressurized Gas Journal Bearings. Bull. JSME, vol. 13, no. 61, July 1970, pp. 873-880.

3. Fleming, D. P.; Cunningham, R. E.; and Anderson, W. J.: Zero-Load Stability of Rotating Externally Pressurized Gas Lubricated Journal Bearings. J. Lub. Tech., vol. 92, no. 2, Apr. 1970, pp. 325-335.

4. Lund, J. W.: A Theoretical Analysis of Whirl Instability and Pneumatic Hammer for a Rigid Rotor in Pressurized Gas Journal Bearings. J. Lub. Tech., vol. 89, no. 2, Apr. 1970, pp. 154-166.

5. Gunter, Edgar J., Jr.: Dynamic Stability of Rotor-Bearing Systems. NASA SP-113, 1966.

6. Kirk, R. Gordon; and Gunter, Edgar J., Jr.: Transient Journal Bearing Analysis. NASA CR-1549, 1970, p. 197.

7. Cunningham, Robert E.; Fleming, David P.; and Anderson, William J.: Experiments on Rotating Externally Pressurized, Air Journal Bearings. I - Load Capacity and Stiffness. NASA TN D-5191, 1969.

8. Lemon, Jason R.: Analytical and Experimental Study of Externally Pressurized Air Lubricated Journal Bearings. J. Basic Eng., vol. 84, no. 1, Mar. 1962, pp. 159-165.

9. Thomson, W. T.: Numerical Methods for Multi-Degree of Freedom System. Vibration Theory and Applications. Prentice-Hall, Inc., 1965, ch. 7.

10. Pan, C. H. T.; and Chiang, T.: Dynamic Behavior of the Spherical Squeeze-Film Hybrid Bearing. J. Lub. Tech., vol. 91, no. 1, Jan. 1969, pp. 149-160.

TABLE I. - BEARING CLEARANCE MEASUREMENTS

(a) Bearing set A: nominal diametral clearance, c_d = 0.003 inch (0.076 mm); orifice diameter, d_o = 0.022 inch (0.056 mm)

Bearing location	Diametral clearances, c_d			
	Preassembled[a]		Assembled	
	in.	mm	in.	mm
Upper	0.00301	0.0765	0.00284	0.0721
Lower	.00305	.0775	.0028	.0711

(b) Bearing set B: nominal diametral clearance, c_d = 0.002 inch (0.051 mm); orifice diameter, d_o = 0.013 inch (0.033 mm)

Upper	0.00203	0.0516	0.00155	0.0394
Lower	.00207	.0525	.00175	.0445

[a]Clearances as determined by subtracting the average rotor diameter, D_r = 2.4999 in. (6.3497 cm) from the average of several bearing inside-diameter measurements prior to assembly.

TABLE II. - PHYSICAL CONSTANTS FOR TEST ROTORS

[Rotor length, L_r = 18 in. (46 cm); average rotor diameter, D_r = 2.4999 in. (6.3497 cm); rotor base material, SAE 52100 consumable-electrode-vacuum-melted steel; surface material, hard chrome plate (ASTM B177-55.]

Rotor number	Construction	Polar moment of inertia, I_p		Transverse moment of inertia, I_t		Mass, m, kg
		lb-in.-sec^2	kg-m^2	lb-in.-sec^2	kg-m^2	
2A	Solid	0.05	0.0056	1.74	0.196	11.13
2B	Solid	.05	.0056	1.74	.196	11.13
2A-H	Hollow	.023	.0026	1.21	.137	7.76

TABLE III. - SUMMARY OF OBSERVED CRITICAL SPEEDS AND

EXPERIMENTALLY DETERMINED FILM STIFFNESSES

(a) Bearing set A: average assembled radial clearance, c = 0.0014 inch (0.036 mm).

Supply pressure ratio, P_o/P_a	System critical speeds, rpm		Instability threshold speed, N_w, rpm	Eccentricity ratio at critical speed		Film stiffness from load-eccentricity data			
						K_{CR1}		K_{CR2}	
	N_{CR1}	N_{CR2}		ϵ_{CR1}	ϵ_{CR2}	lbf/in.	N/m	lbf/in.	N/m
Upper bearing									
3.0	13 200	15 000	21 950	0.14	0.14	94.5×10^3	166×10^5	93.5×10^3	164×10^5
4.2	16 600	20 300	25 700	.21	.22	170	298	165	289
5.6	19 000	23 500	26 850	.26	.26	227	397	227	397
6.8	21 300	25 600	28 000	.26	.24	300	525	302	529
Lower bearing									
3.0	12 000	17 500	21 950	0.05	0.07	98×10^3	171×10^5	97×10^3	170×10^5
4.2	16 500	21 500	25 700	.11	.11	170	298	170	298
5.6	19 000	24 000	26 850	.16	.14	250	437	254	445
6.8	21 000	26 000	28 000	.17	.11	280	490	286	500

(b) Bearing set B: average assembled clearances - upper bearing, c = 0.0008 inch (0.020 mm); lower bearing, c = 0.0009 inch (0.023 mm)

Supply pressure ratio, P_o/P_a	System critical speed, N_{CR1}, rpm	Instability threshold speed, N_w, rpm	Eccentricity ratio at critical speed, ϵ_{CR1}	Film stiffness from load-eccentricity data, K_{CR1}	
				lbf/in.	N/m
Upper bearing					
2.3	18 000	21 500	0.11	135×10^3	236×10^5
3.0	19 500	25 300	.19	177	310
3.6	20 500	27 000	.24	250	438
4.8	21 300	27 700	.39	283	495
6.1	23 200	27 300	.54	330	577
7.4	24 500	26 600	.57	420	735
Lower bearing					
2.3	11 500	21 500	0.02	113×10^3	198×10^5
3.0	15 000	25 300	.02	186	326
3.6	17 000	27 000	.05	260	455
4.8	21 000	27 700	.16	392	685
6.1	22 800	27 300	.25	422	738
7.4	24 000	26 600	.31	552	964

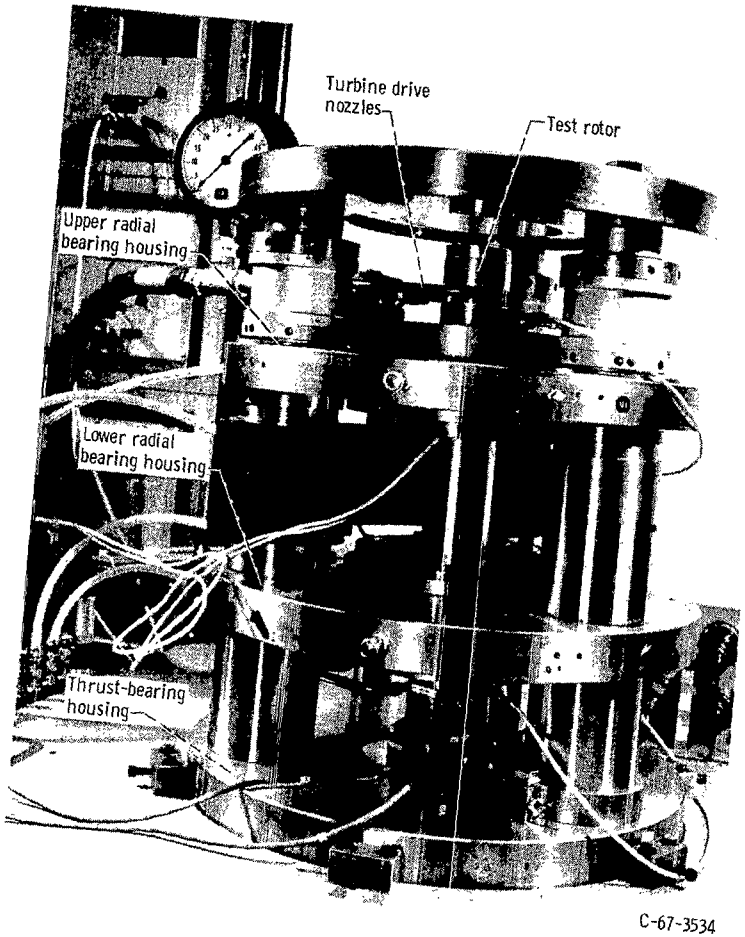

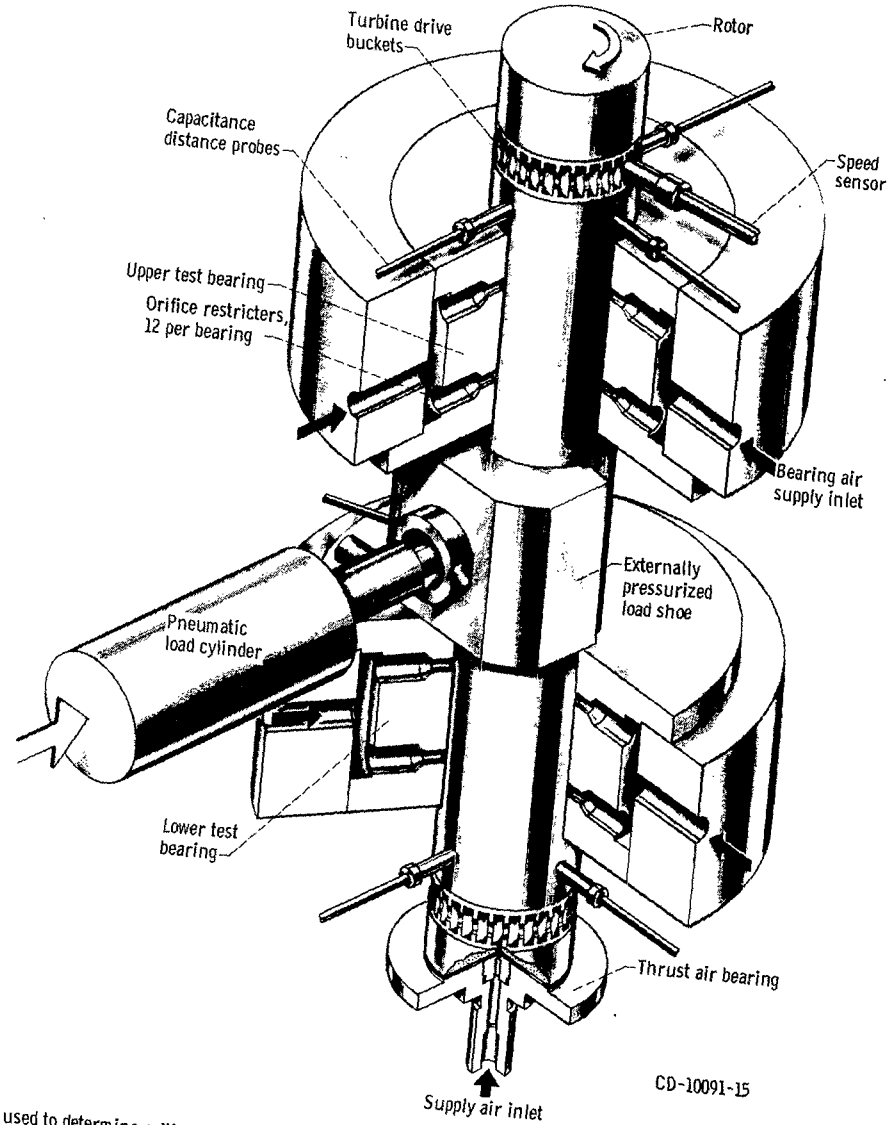

Figure 1. - Test apparatus used to determine critical speeds.

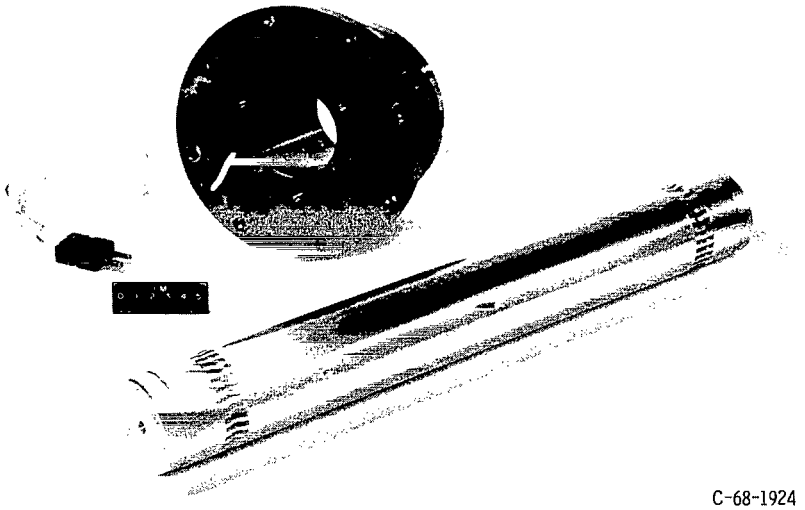

C-68-1924

Figure 2. - Externally pressurized air bearing and test rotor.

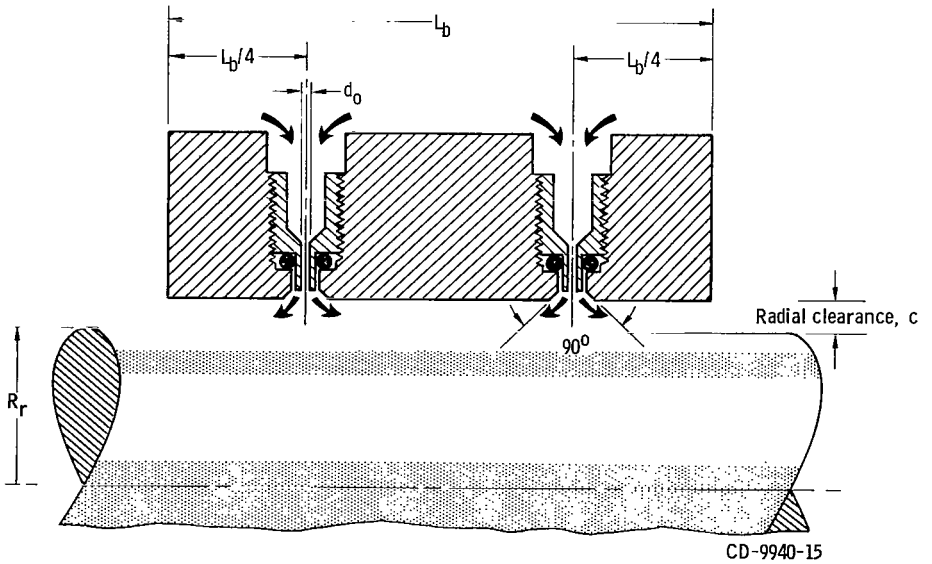

Figure 3. - Section view of test bearing.

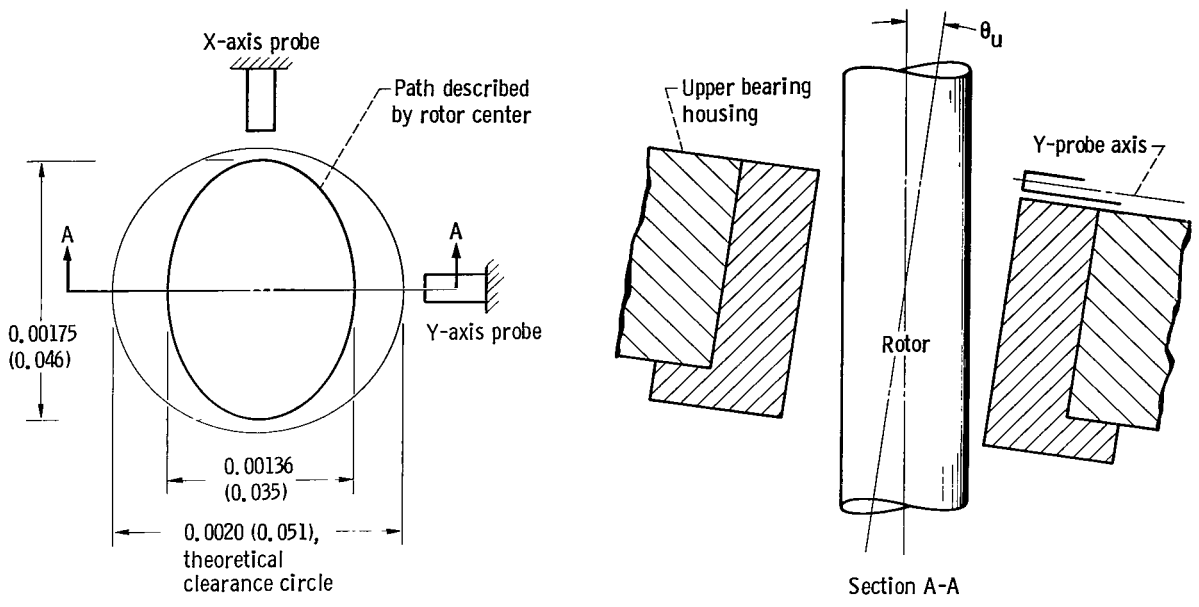

(a) Upper bearing.

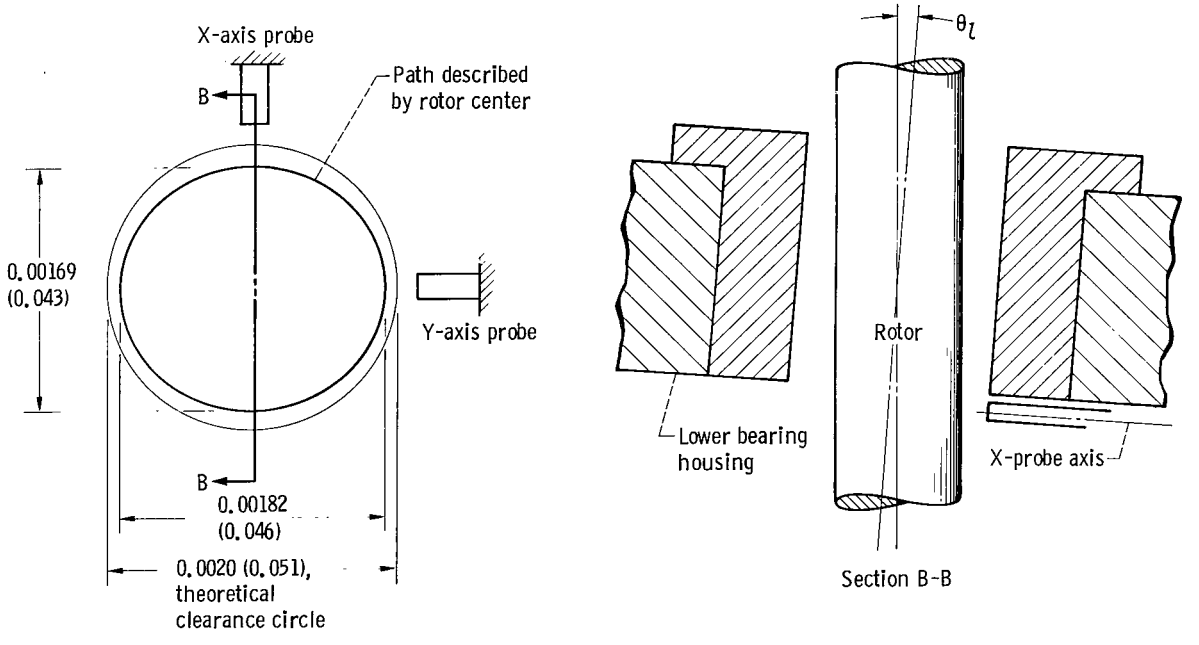

(b) Lower bearing.

Figure 4. - Schematic representation of misalinement in assembly of bearing set B. (Dimensions are in inches (mm).)

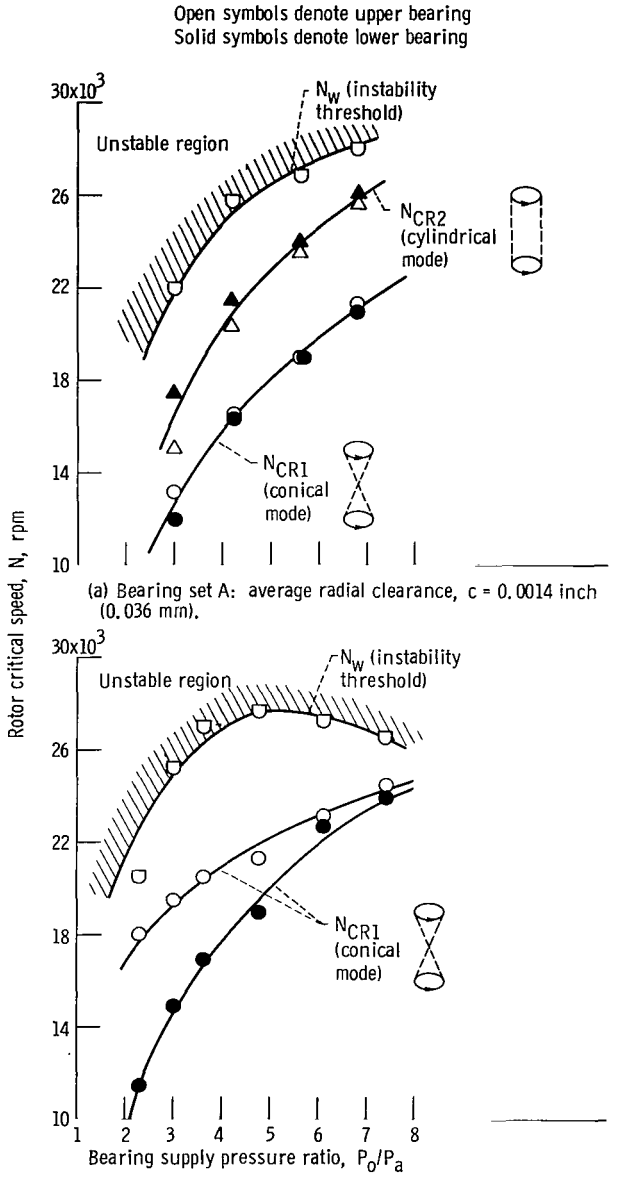

(a) Bearing set A: average radial clearance, c = 0.0014 inch (0.036 mm).

(b) Bearing set B - radial clearances: upper bearing, c = 0.0008 inch (0.020 cm); lower bearing, c = 0.009 inch (0.023 cm).

Figure 5. - Rotor critical speeds and instability threshold as function of bearing supply pressure ratio.

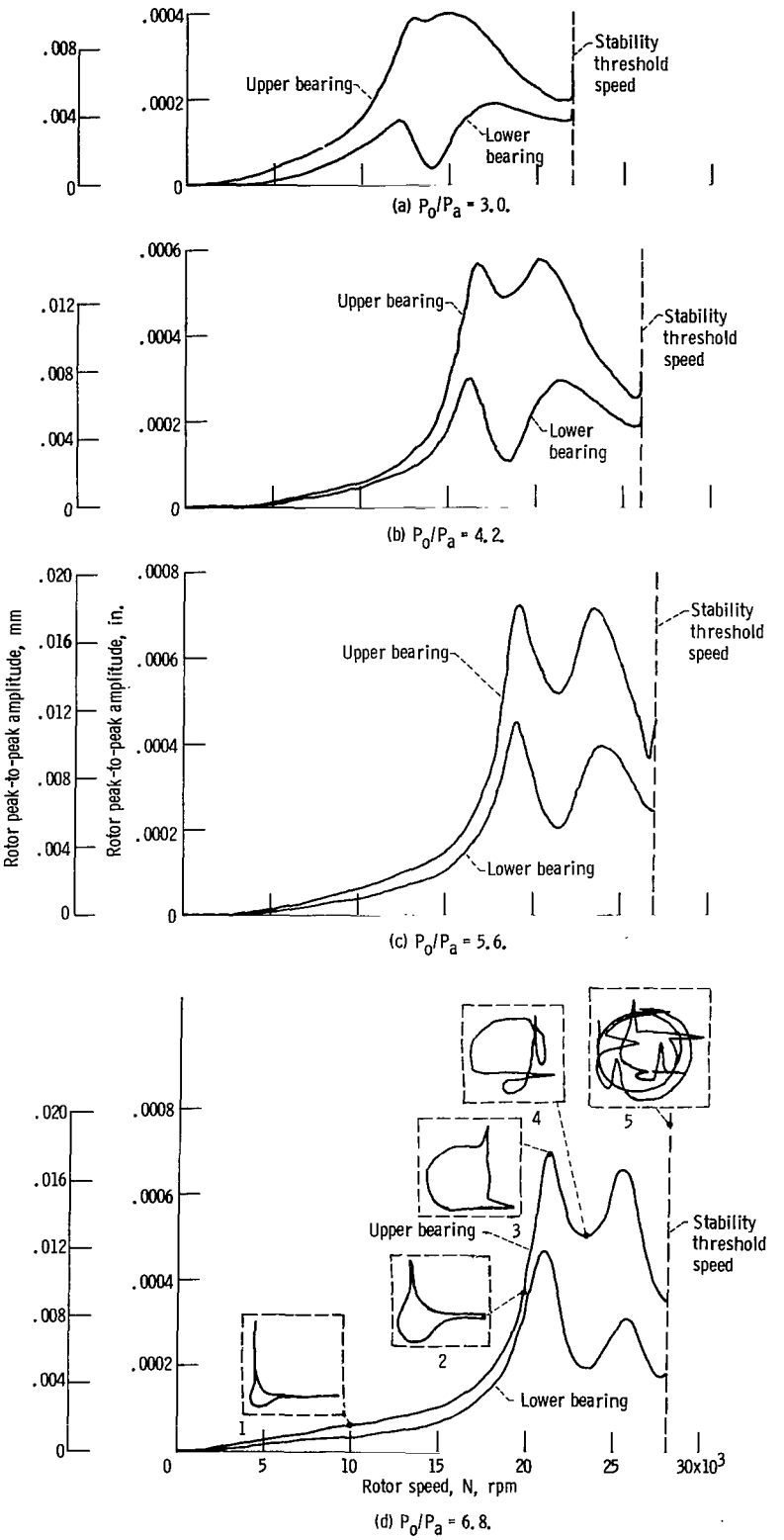

Figure 6. - Rotor amplitude as function of rotor speed at varying supply pressure ratios P_0/P_a. Bearing set A: average radial clearance, c = 0.0014 inch (0.036 cm).

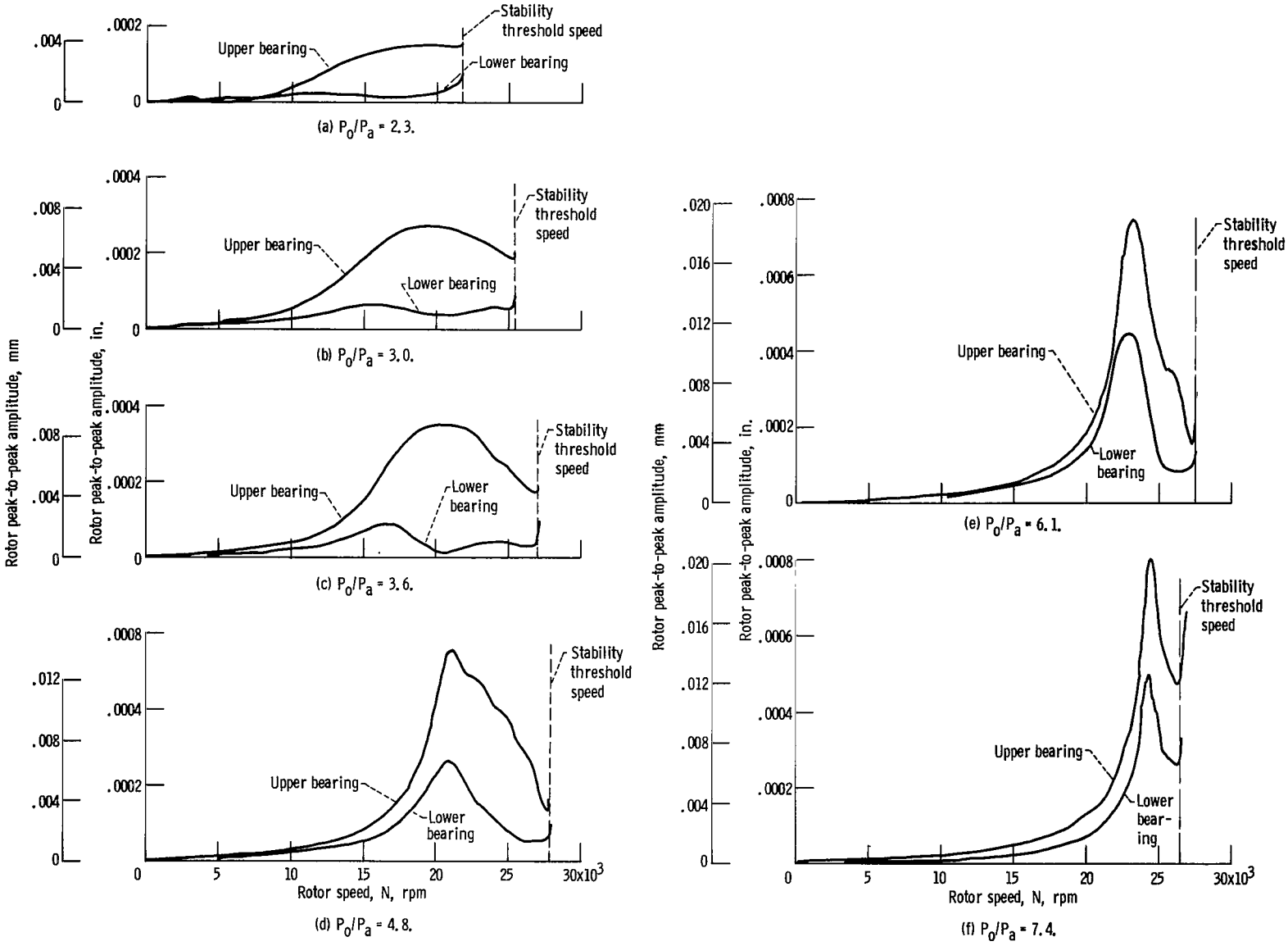

Figure 7. - Rotor amplitude as function of rotor speed at varying supply pressures P_0/P_a. Bearing set B - radial clearances: upper bearing, c = 0.0008 inch (0.020 mm); lower bearing, c = 0.0009 inch (0.023 mm).

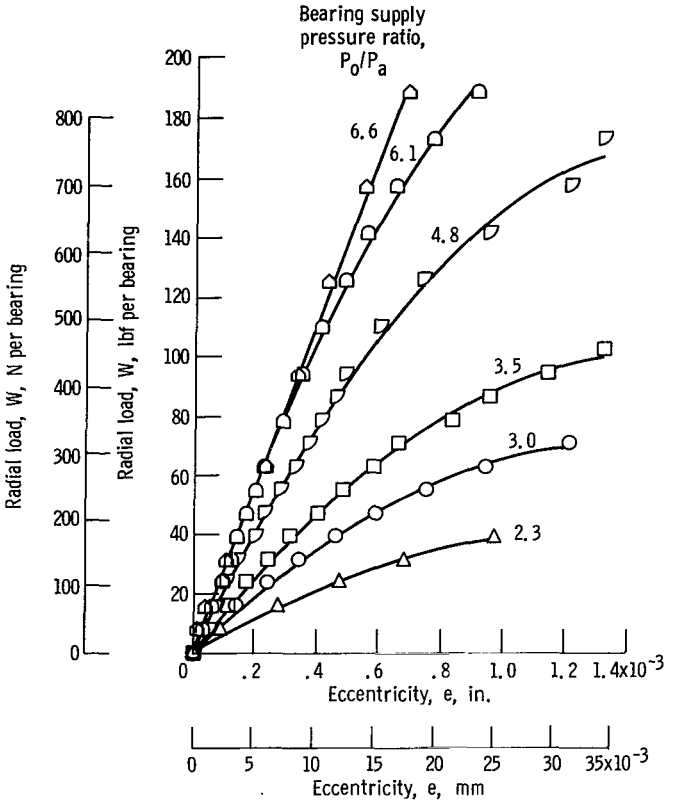

Figure 8. - Radial load as function of eccentricity at varying bearing supply pressure ratios at rotor speed N = 0. Bearing set A: radial clearance, c = 0.0014 inch (0.036 mm); atmospheric pressure, P_a = 14.73 psia (101.3 kN/m^2).

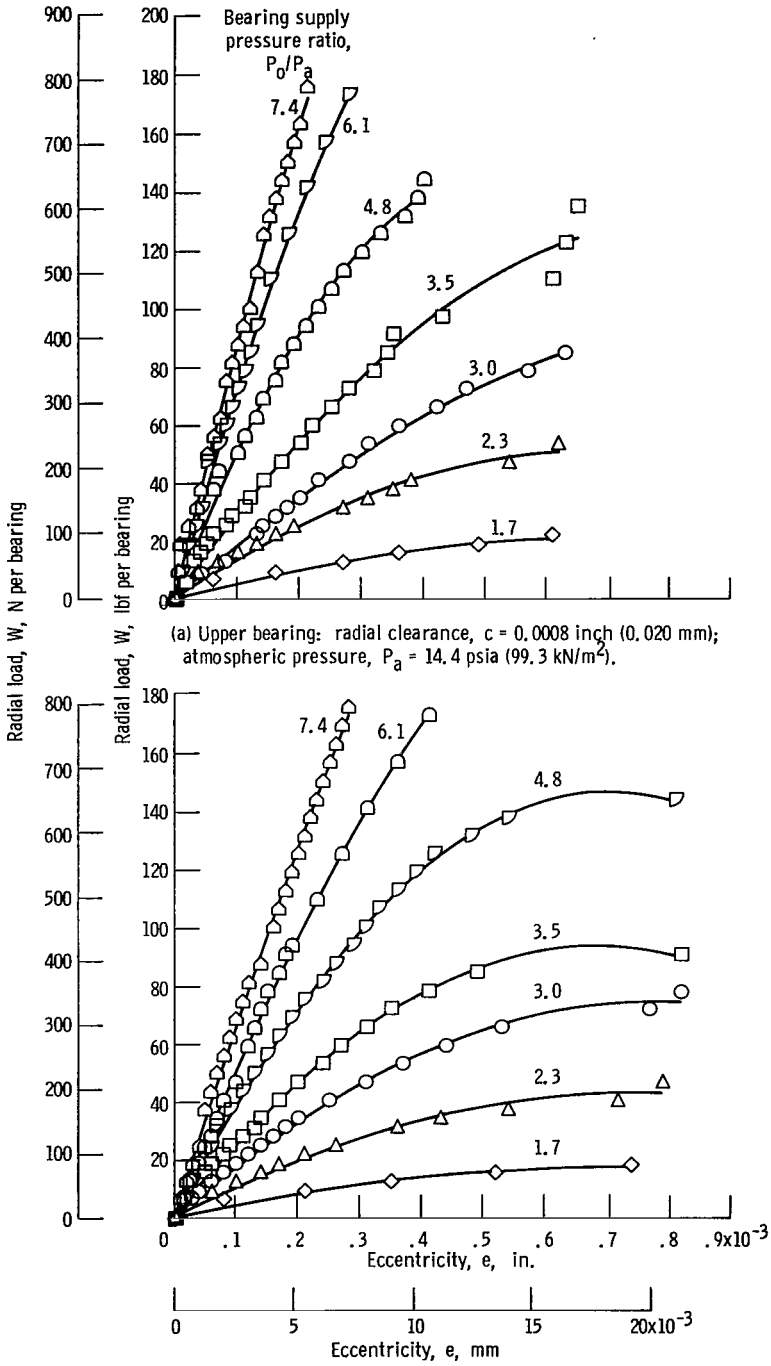

(a) Upper bearing: radial clearance, c = 0.0008 inch (0.020 mm); atmospheric pressure, P_a = 14.4 psia (99.3 kN/m^2).

(b) Lower bearing: radial clearance, c = 0.009 inch (0.023 cm); atmospheric pressure, P_a = 14.7 psia (101 kN/m^2).

Figure 9. - Radial load as function of eccentricity at varying bearing supply pressure ratios at rotor speed N = 0. Bearing set B.

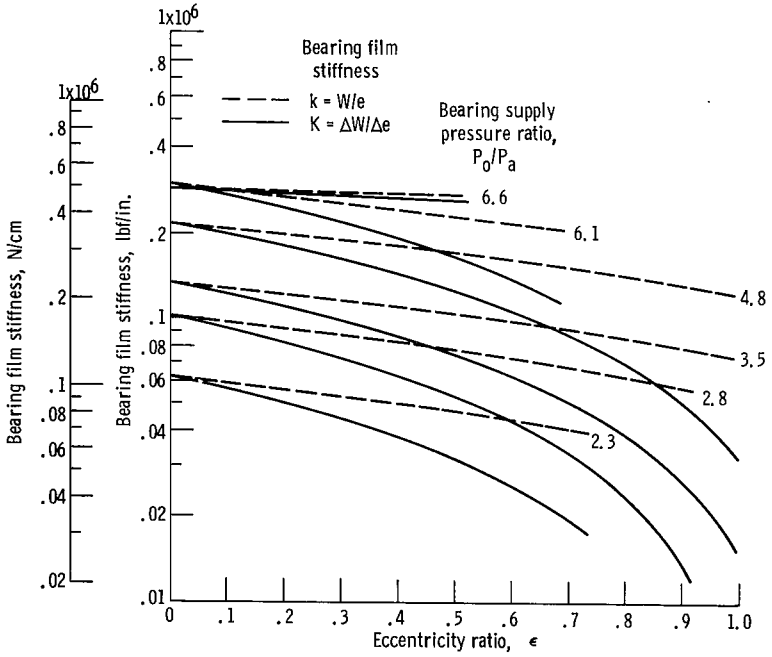

Figure 10. - Bearing static film stiffness as function of eccentricity ratio at varying supply pressure ratios. Bearing set A: average radial clearance, c = 0.0014 inch (0.036 mm).

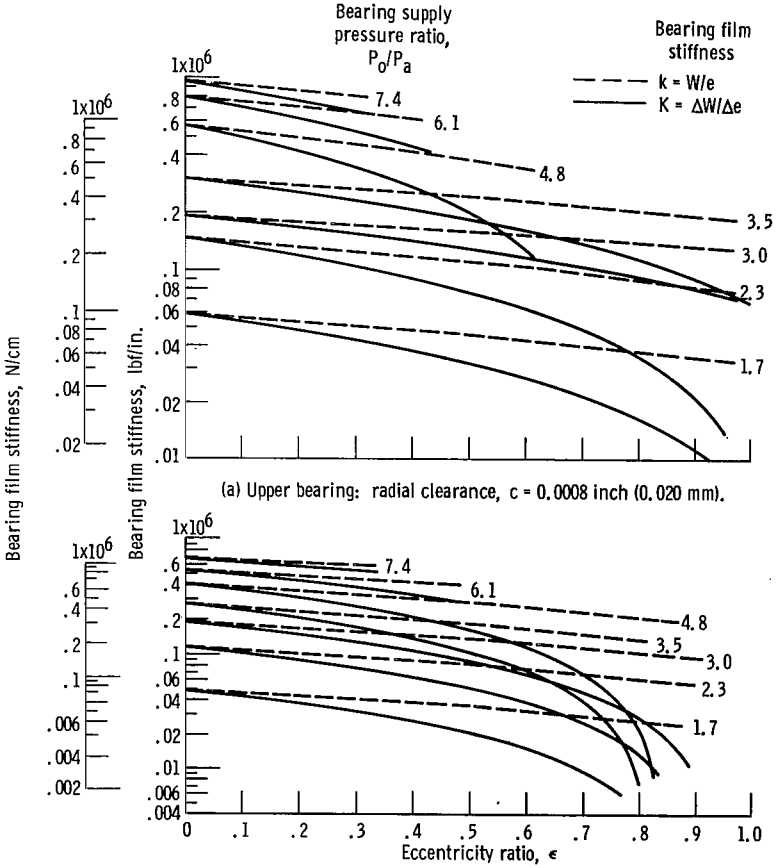

(a) Upper bearing: radial clearance, c = 0.0008 inch (0.020 mm).

(b) Lower bearing: radial clearance, c = 0.0009 inch (0.023 mm).

Figure 11. - Bearing static film stiffness as function of eccentricity ratio at varying supply pressure ratios. Bearing set B.

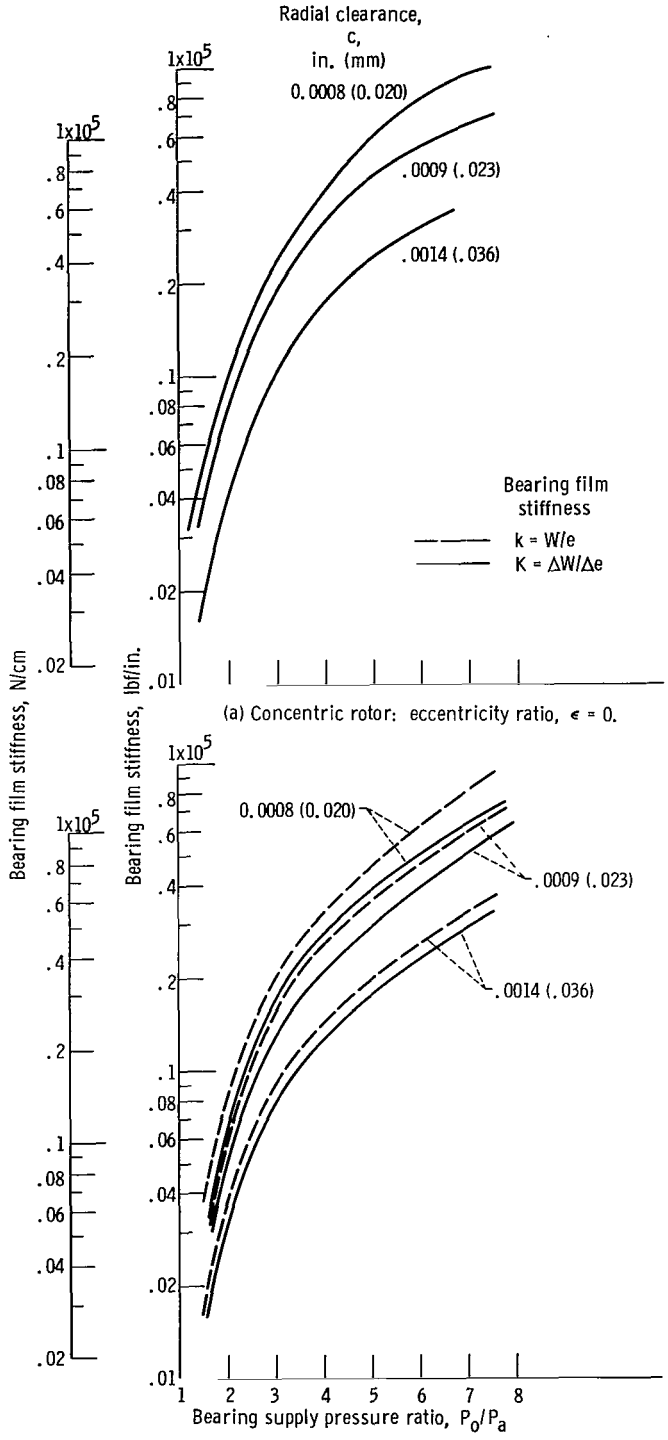

Figure 12. - Bearing static film stiffness as function of supply pressure ratio at different values of radial clearance.

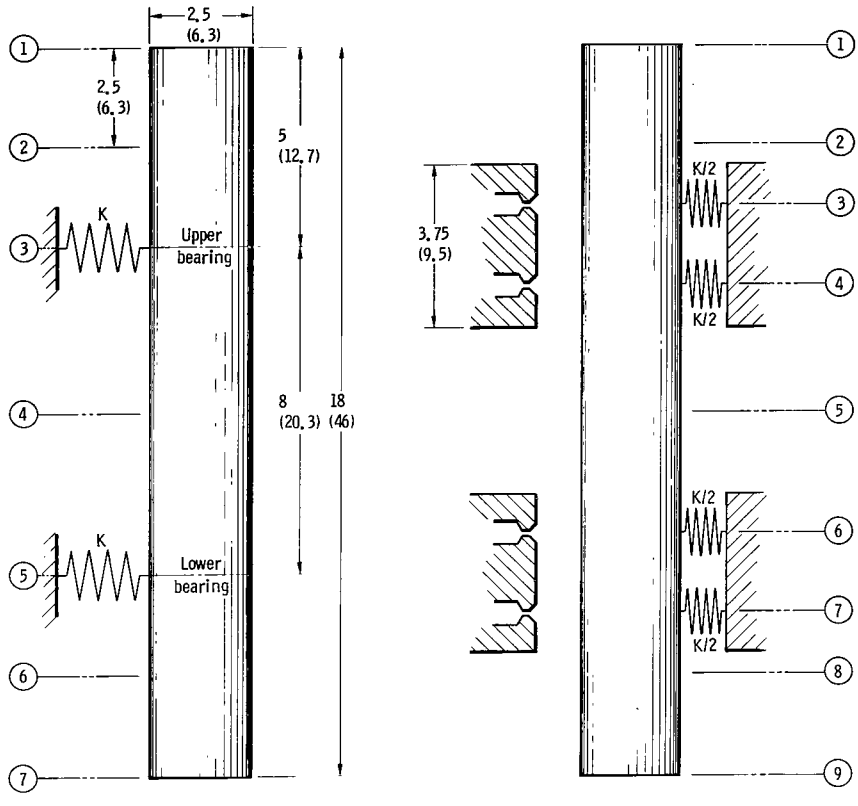

(a) Lumped bearing: seven mass stations.

(b) Distributed bearing: nine mass stations.

Figure 13. - Comparison of rotor bearing models used in dynamics analysis. (Dimensions are in inches (cm).)

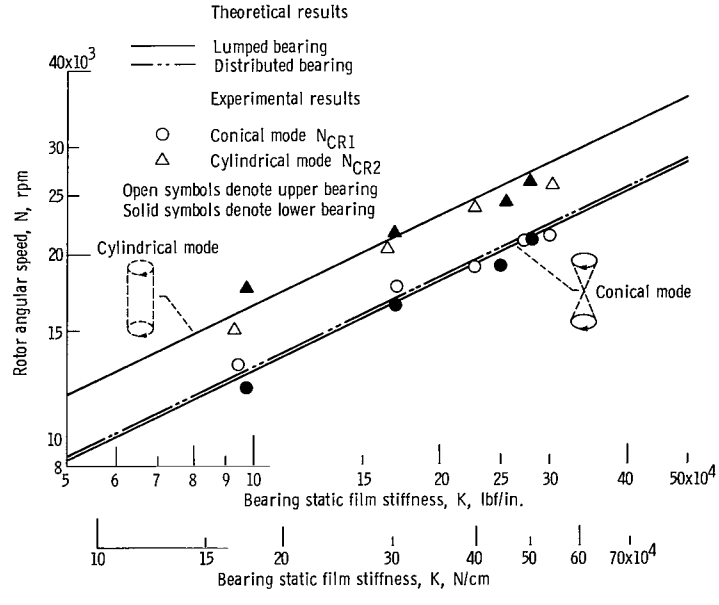

Figure 14. - Rotor critical speeds as function of bearing static film stiffness for bearing set A. Average assembled radial clearance, c = 0.0014 inch (0.036 mm).

NATIONAL AERONAUTICS AND SPACE ADMINISTRATION
WASHINGTON, D.C. 20546

OFFICIAL BUSINESS
PENALTY FOR PRIVATE USE $300

FIRST CLASS MAIL

POSTAGE AND FEES PAID
NATIONAL AERONAUTICS AN
SPACE ADMINISTRATION

12U 001 40 51 3DS 71118 00903
AIR FORCE WEAPONS LABORATORY /WLOL/
KIRTLAND AFB, NEW MEXICO 87117

ATT E. LOU BOWMAN, CHIEF,TECH. LIBRARY

POSTMASTER: If Undeliverable (Section 158 Postal Manual) Do Not Return

"The aeronautical and space activities of the United States shall be conducted so as to contribute . . . to the expansion of human knowledge of phenomena in the atmosphere and space. The Administration shall provide for the widest practicable and appropriate dissemination of information concerning its activities and the results thereof."

—NATIONAL AERONAUTICS AND SPACE ACT OF 1958

NASA SCIENTIFIC AND TECHNICAL PUBLICATIONS

TECHNICAL REPORTS: Scientific and technical information considered important, complete, and a lasting contribution to existing knowledge.

TECHNICAL NOTES: Information less broad in scope but nevertheless of importance as a contribution to existing knowledge.

TECHNICAL MEMORANDUMS: Information receiving limited distribution because of preliminary data, security classification, or other reasons.

CONTRACTOR REPORTS: Scientific and technical information generated under a NASA contract or grant and considered an important contribution to existing knowledge.

TECHNICAL TRANSLATIONS: Information published in a foreign language considered to merit NASA distribution in English.

SPECIAL PUBLICATIONS: Information derived from or of value to NASA activities. Publications include conference proceedings, monographs, data compilations, handbooks, sourcebooks, and special bibliographies.

TECHNOLOGY UTILIZATION PUBLICATIONS: Information on technology used by NASA that may be of particular interest in commercial and other non-aerospace applications. Publications include Tech Briefs, Technology Utilization Reports and Technology Surveys.

Details on the availability of these publications may be obtained from:

SCIENTIFIC AND TECHNICAL INFORMATION OFFICE

NATIONAL AERONAUTICS AND SPACE ADMINISTRATION

Washington, D.C. 20546